4

Ultra-wideband 32-Element 3D-MIMO Antenna for Vehicular Applications

A wideband 32-element vehicular 3D-MIMO system is proposed by utilizing eight-element MIMO antenna for Internet-of-Vehicle/Vehicle-to-Everything, in this chapter. The eight-element MIMO antenna consists of four sets of two identical same oriented antenna elements are placed in orthogonal symmetric fashion on the top of an octagon-shaped substrate board. A combination of ground stubs between two same oriented antenna is loaded with shared ground at the bottom of the same substrate for better matching and low correlation, which are fed through the tapered microstrip line. Similarly, dual I-shaped stubs interconnected with shared ground for high isolation between a pair of corner elements. The proposed antenna achieved measured impedance bandwidth ($S_{ij} \in i=j < -10$ dB) of 3.03-15.33 GHz with a minimum isolation value ($S_{ij} \in i \neq j$) of 15.5 dB. Furthermore, an eight-element MIMO antenna with the extended ground is vertically orthogonally symmetrically rotated around the central axis, forming a 32-element 3D-MIMO antenna system. The performances of the 3D-MIMO antenna with radome and large metallic sheet are also examined, and satisfactory results are observed for 3D system-in-package *

*Parts of this chapter is under review: Arun Kumar Saurabh and Manoj Kumar Meshram, "Wideband 32-element 3D-MIMO antenna for vehicular applications," *IEEE Transactions on Vehicular Technology.*

4.1 Introduction

The need of new features in the vehicle is growing day to day. As a result, modern vehicles/automotive cars are equipped with the latest technologies that make people's lives more convenient. Fig. 4.1. illustrates advanced vehicular communication, where vehicles are communicated with 5G Sub-6 GHz V2P (Vehicle-to-Person, 3.3-4.2 GHz/3.3-3.8 GHz/4.4-5.0 GHz), WLAN (in the vehicle Driver's-to-Passengers, 5.1-5.9 GHz), V2X (Vehicle-to-Everything, 5.8-5.925 GHz), V2V/V2I (Vehicle-to-Vehicle/Vehicle-to-Infrastructure, 5.85-5.925 GHz), also with Vehicle-to-Satellite communication (X-band 7/8 GHz, Ku-band 12/14 GHz) for intelligent Internet of Vehicles (IoV). To perform those coexisting network communication, the vehicle antenna should be needed high-speed signal quality, multiple network connections by utilizing multiple antennas in multipath environments, and multiple frequency bands active at the same time. Therefore, the demand for the embodiment of multiple antennas in place of a single antenna with reasonable correlation in the vehicles is rapidly increasing for modern vehicular communication.

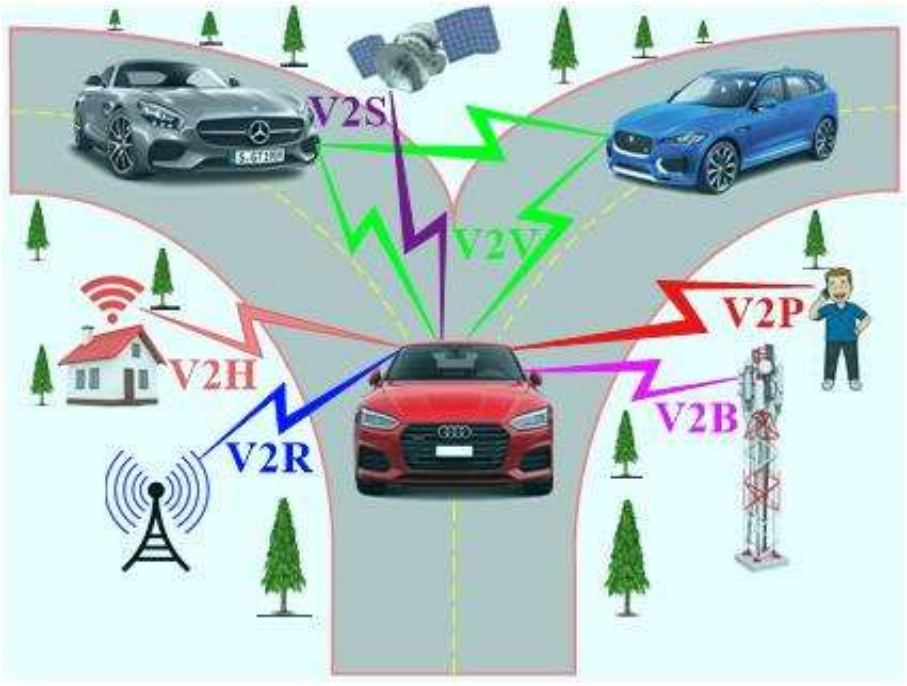

Fig. 4.1: Modern vehicular wireless communication in IoV/V2X.

The designer's primary constraints are the packaging and installing the vehicular MIMO antenna because the convenient space available for embedding multiple antennas is minimal. To diminish the total size of the MIMO antenna, the design antenna elements should be closely placed, low-profile, and compact. Due to this, the correlation between antenna elements is highly increased. Achieving and maintaining low correlation through a shared ground plane between closely positioned higher-order MIMO antenna elements are another primary constraint and more challenging throughout the covered wideband than the narrow frequency band. Hence, a wideband higher-order MIMO antenna is the best substitute to cover those performances in vehicular communication. This type of antenna design is a challenging task for the designer.

Some vehicular antenna designs have been proposed in recent years to overcome the aforementioned issues in modern vehicular communication. In [123], a V-shaped slot-loaded triangular patch antenna with a circular ground was designed for V2V and WLAN applications. Similarly, for V2V and WLAN, the stacked circular patch configuration was utilized for dual-band operation having the annular ring and vias for bandwidth enhancement [124]. In [125], a hexagonal fern fractal 3D antenna surrounded by dielectric substrate placed at metal block was proposed for blind spot detection (IEEE802.11y band). Stubs and concave loaded dual-band 3D circular metal antenna having dual circular polarization were designed for V2S and V2B (vehicle-to-basestation) [126]. In [55], two orthogonal monopole antennas were utilized to configure a two-element UWB-MIMO antenna for in-car communication. Similarly, in [127] optically transparent monopole antenna was used to design a two-element MIMO antenna. Two orthogonal dipole antenna was utilized to configure a 3D-MIMO antenna for IoV. It consists of parasitic elements for wider bandwidth and the artificial magnetic conductor (AMC) cavity and metallic wall for gain enhancement [128]. In [129]-[130], a single slot-

based antenna was vertically rotated around the centre axis at the interval of 90^0 to configure the quad-element 3D-MIMO antenna for vehicular environment communication. A set of ring dielectric resonator antenna pairs was placed 180^0 out of phase to create the quad-element 3D-MIMO antenna for beam tilting application. The metallic wall was designed to reduce the coupling between DRA elements [131]. A wideband quad-element 3D-MIMO antenna was proposed for 5G sub-6 GHz, LTE, WLAN, and V2X communication. A tapered dielectric-loaded horn was orthogonally arranged around the centre of the circular plate, and it also consists of annular slots and vias for wider bandwidth [132]. In [133], a vertically polarized monopole antenna was orthogonally rotated around the central axis to create the quad-element 3D-MIMO antenna for the vehicular basestation. Similarly, in [134], a dual-polarized metasurface lens-loaded Vivaldi antenna was utilized to configure a wideband quad-element 3D-MIMO antenna. It consists of DR-loaded radome and EM reflector for gain enhancement. A set of quad-element MIMO antennas was utilized to create an eight-element MIMO array. In [135], the cavity model was proposed for mounting the vehicular antenna in the automotive's front, centre, and end rear roof. However, the discussed antenna designs in [123]-[126], [55], [127]-[128], [129]-[133], and [134] are 1-, 2-, 4-, and 8-element, respectively, and some of them are only covered narrowband and/or dual communication band at a time. Therefore, a wideband higher-order MIMO antenna with high isolation and high gain is needed for modern automotive communication.

In this chapter, a novel compact wideband 32-element 3D-MIMO antenna design is investigated to resolve the aforementioned issues. The wideband 32-element 3D-MIMO antenna consists of four sets of eight-element MIMO antenna with the extended ground. A compact, low-profile wideband eight-element MIMO antenna is vertically symmetrically rotated 90^0 around to central axis for configuring a 32-element 3D-MIMO

system for wireless vehicular communications. Further, the investigation is carried out by keeping the antenna system inside the radome and placed on the vehicle's roof-top. The vehicle roof-top consists of a large metallic sheet in the simulation study. The configured 3D-MIMO system has successfully maintained satisfactory performances; it may apply to embed the host in a practical vehicular system-in-package which is the advantage of the present proposal.

4.2 Details of MIMO Antenna

The eight-element MIMO antenna is configured on an octagon-shaped cross-section area of 4287.5 mm^2 [(L_A×L_A) – (1/2×L_R×L_R)4] or about 0.4374 λ_0^2, (where λ_0 is the highest operating wavelength at the lowest frequency 3.03 GHz) of the FR4-epoxy substrate (ε_r=4.4, *tan* δ=0.02, thickness t=0.8mm). The final configuration with dimension parameters is illustrated in Fig. 4.2, which is referred as confi_1 for further study.

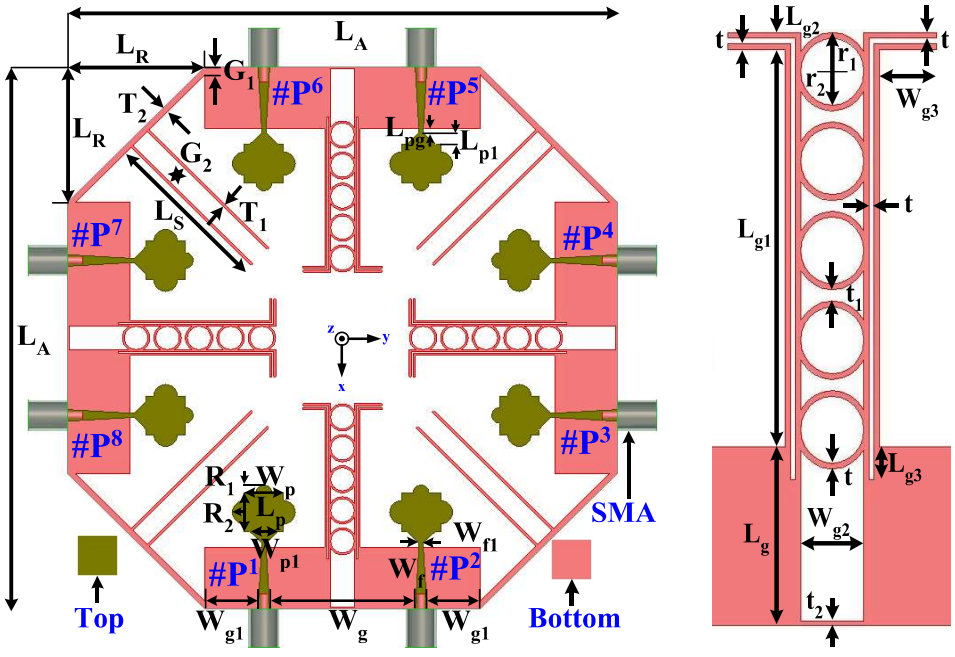

(a) (b)

Fig. 4.2: Eight-element MIMO antenna (a) configuration, (b) zoomed view of stub. Dimensions (*in mm*): L_A=70, L_R=17.5, L_g=8, L_{g1}=17.75, L_{g2}=0.75, L_{g3}=1.5, W_g=18.5, W_{g1}=6.75, W_{g2}=3, W_{g3}=2.75, t=0.25, t_1=0.5, t_2=0.2, r_1=1.75, r_2=1.5, T_1=0.3, T_2=0.7, G_1=1, G_2=2.52, L_S=21.5, L_p=5, L_{p1}=1.5, W_p=5, W_{p1}=3.6, W_f=1.5, W_{f1}=0.5, R_1=1, R_2=1.5, L_{pg}=0.5.

4.2.1 Design Evolution of Eight-Element MIMO Antenna

The design evolution of the antenna preliminary starts by selecting a simple planar square-shaped monopole element fed through a microstrip line for achieving UWB performance. The proposed radiating element consists of the combination of square-shaped (L_p, W_p), three half-circle (R_1, R_2), and trapezium-shaped (L_{p1}, W_{p1}, W_{f1}), which is fed through tapered microstrip line width of W_f for better impedance matching having a rectangular ground plane. The two identical radiating elements are placed in the same orientation, having a shared ground plane on a substrate cross-section area of $0.26\lambda_0 \times 0.35\lambda_0$ or 26.5×35 mm^2; they are formed two-element MIMO antenna, as illustrated in Fig. 4.3(a). The edge-to-edge minimum distance between two-element is less than $\lambda_0/8$ ($0.121\lambda_0$) for compact MIMO configuration. A combination of the ground stub (ring connected slit loaded inverted L-shaped strip) is connected to a shared ground to achieve simultaneous better impedance matching and high isolation between element-1 (#P^1) and element-2 (#P^2). It provides a -10 dB reflection coefficient ($S_{11} \in i=j$) of 5.0-26.5 GHz and the coupling coefficient ($S_{21} \in i \neq j$) better than -18.25 dB between antenna elements, as shown in Fig. 4.3(b).

Further, the two-element MIMO antenna is arranged in orthogonal symmetric fashion on the top of the octagon-shaped substrate's board. An interconnected ground is configured on the same substrate's bottom side, forming an eight-element MIMO antenna. The edge-to-edge minimum distance between two closely-spaced corner elements is also less than $\lambda_0/8$ ($0.107\lambda_0$). To reduce the correlation mainly between corner elements like element-1 (#P^1) and element-8 (#P^8) etc., dual I-shaped stubs are interconnected to the shared ground. Finally, the presented eight-element MIMO antenna successfully obtained wideband performance with good isolation value going through the optimized design evaluation. It achieved the simulated impedance bandwidth ($S_{ij} \in i=j <$

−10 dB) of 3.03-16 GHz with a minimum isolation value ($S_{ij} \in i \neq j$) of 15.5 dB in the respective band.

4.2.2 Fundamental Resonant Frequency

The fundamental lower resonant frequency of the configured MIMO antenna is approximated using following equation.

$$f_r = \frac{144}{l_g + l_{rp} + g_{grp} + \frac{A_g}{2\pi l_g \sqrt{\varepsilon_{reff}}} + \frac{A_{rp}}{2\pi l_{rp} \sqrt{\varepsilon_{reff}}}} \quad \text{GHz} \qquad (4.1)$$

where,

$l_g = L_g + L_{g1} + L_{g2}$,

$l_{rp} = R_1 + L_p + L_{p1}$,

$g_{grp} = L_{pg}$,

$A_g \cong [4\{(W_g+2W_f+2W_{g1})L_g - (L_g-t_2)W_{g2} - 2L_{g3}t + 2\{(L_{g1}+t)t + tW_{g3}\} + 2\{(L_{g1}+L_{g2})t + (2t+W_{g3})t\} + 5\pi(r_1^2-r_2^2)\} + 4(\sqrt{2}L_R T_2 - G_1^2/2) + 8L_S T_1]$,

$A_{rp} = [\pi R_1^2/2 + \pi R_2^2 + L_p W_p + L_{p1}\{(W_{p1}+W_{f1})/2\} + (L_{pg}+L_g)\{(W_{f1}+W_f)/2\}]$.

The fundamental lower resonant frequency of the configured single antenna element of the MIMO antenna is calculated with the help of the Eq. (4.1) and obtained value of the lower resonant frequency (f_r) is 3.63 GHz.

Fig. 4.4 shows the real and imaginary part of input impedance with respect to frequency for the configured MIMO antenna. The value of input impedance at the frequency of 3.4 GHz is observed almost close to (50+j0) Ω. Which indicates that the simulated first resonating frequency is nearly close to the calculated value.

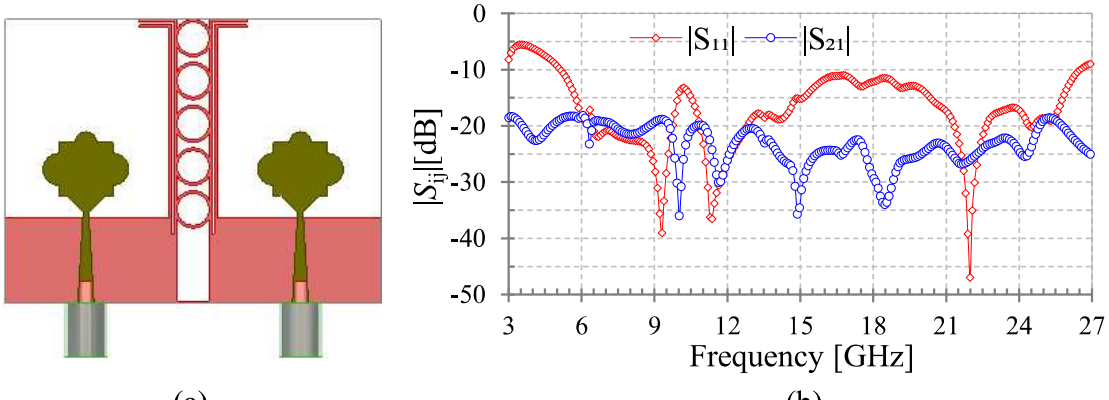

(a) (b)

Fig. 4.3: Two-element MIMO antenna (a) configuration, (b) corresponding *S*-parameters.

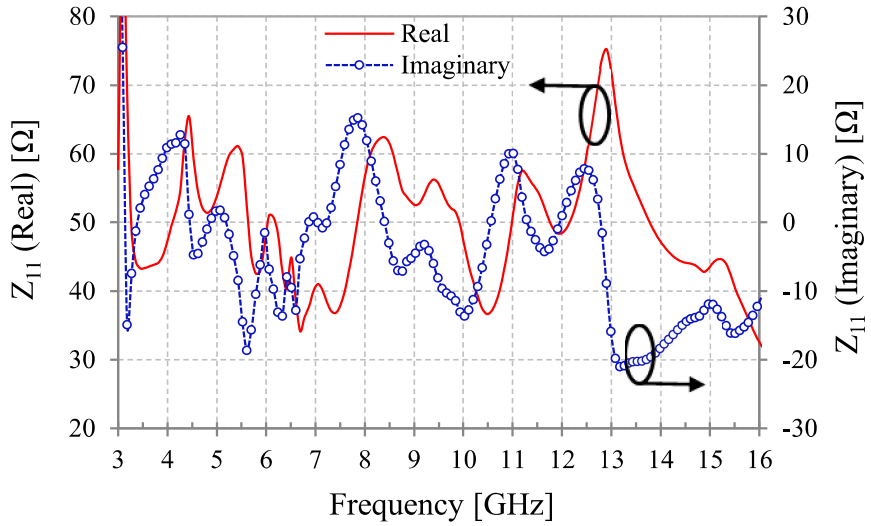

Fig. 4.4: Input impedance for element-1 of the eight-element MIMO antenna.

4.2.3 Effect of Decoupling Structures on Shared Ground

To understand the effectiveness of ground stubs as a decoupling structure, the current distribution is plotted on the surface of the antenna's ground and elements at 6.7 GHz by keeping element-1 excited, and the rest of all elements kept matched terminated, as illustrated in Fig. 4.5. In Fig. 4.5(a), it is observed that without any decoupling structures on the shared ground, the orientation of the coupling current is highly concentrated on the whole ground, mainly toward neighboring element-2 (#P^2) and element-8 (#P^8) and resulted in poor S_{ij}-parameter performances. Fig. 4.5(b) shows a combination of the ground strip is placed between two identical antenna elements, i.e., element-1 (#P^1) and element-2 (#P^2). The orientation of surface current is highly concentrated on the combination of the ground strip, decreasing the coupling current mainly from element-1 (#P^1) to element-2 (#P^2). However, some part of the coupling current still flows from element-1 (#P^1) to element-8 (#P^8), and the resulting isolation between element-1 (#P^1) and element-2 (#P^2) improved. Furthermore, a dual I-shaped ground strip is placed between two corner antenna elements, i.e., element-1 (#P^1) and element-8 (#P^8), as illustrated in Fig. 4.5(c). The orientation of surface current is highly concentrated on dual I-shaped strip and the combination of the ground strip on the shared ground, therefore

decreasing the coupling current from element-1 (#P[1]) to element-2 (#P[2]) and element-8 (#P[8]). Hence, 15.5 dB minimum isolation ($S_{ij} \in i \neq j$) is successfully achieved throughout the covered band between a pair of antenna elements with better impedance matching ($S_{ij} \in i=j$ < -10 dB).

4.3 Results and Discussion

The performances of the proposed eight-element MIMO antenna are analyzed in the following sections.

4.3.1 *S*-parameters

The prototype (top and bottom view) of the proposed antenna is illustrated in Fig. 4.6(a)-(b), corresponding simulated and measured *S*-parameters plots are shown in Fig. 4.6(c)-(d). All radiating elements are identical in the presented MIMO configuration. All other reflection *S*-parameters are identical to the S_{11}, and all other coupling *S*-parameters are almost similar to the S_{12}, S_{13}, S_{14}, S_{15}, S_{16}, S_{17}, and S_{18}. The proposed MIMO antenna has a measured $S_{ij} \in i=j$ < -10 dB frequency range of 12.3 GHz (3.03-15.33 GHz) and a minimum isolation value $S_{ij} \in i \neq j$ of 15.5 dB between a pair of elements throughout the wideband. The measured results of the prototype are almost analogous to the simulated, and minor discrepancies occurred mainly due to fabrication and soldering tolerances.

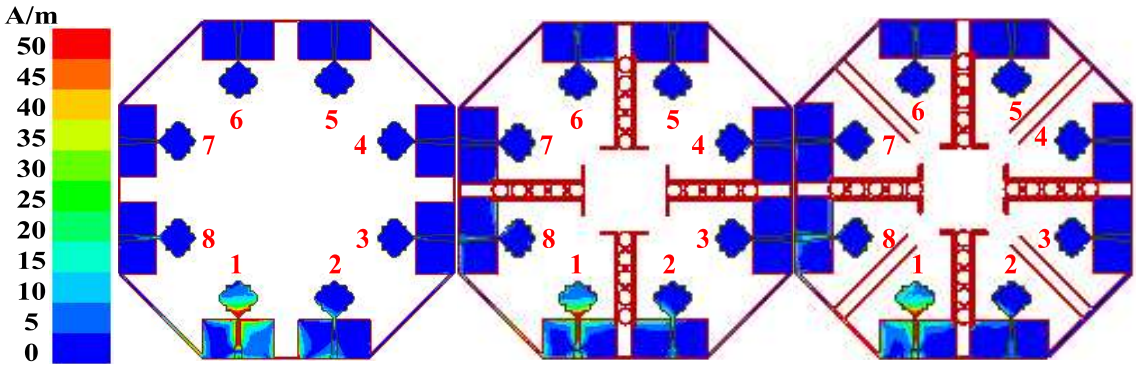

(a) (b) (c)

Fig. 4.5: Surface current distribution on the shared ground (a) without any strip, (b) with a combination of strip, and (c) another dual I-shaped strip.

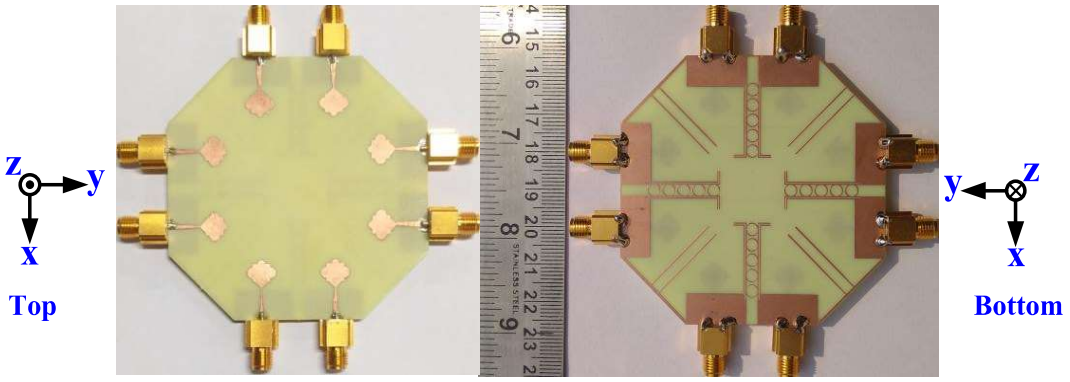

(a) (b)

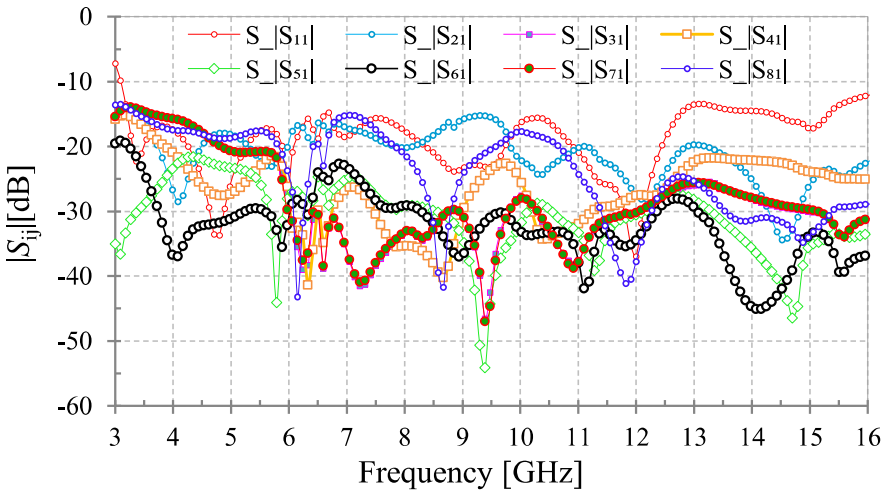

(c)

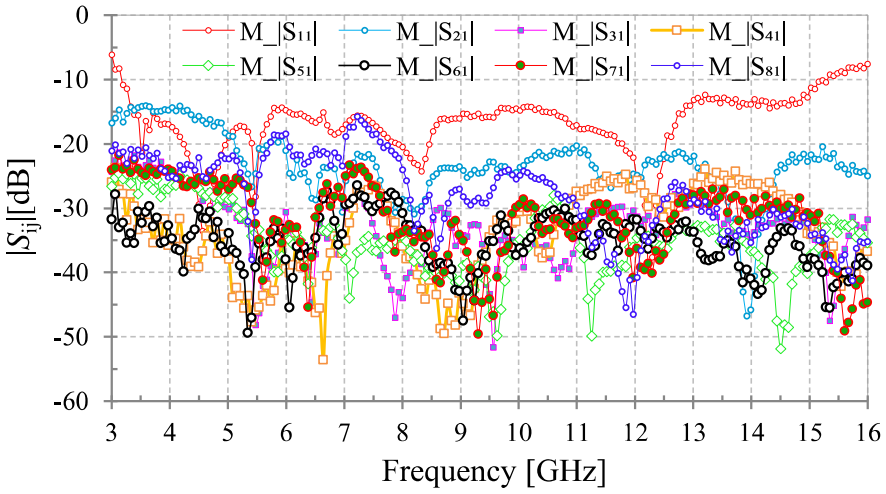

(d)

Fig. 4.6: (a) Top view, (b) bottom view, (c) simulated *S*-parameters, and (d) measured *S*-parameters of the eight-element MIMO antenna.
Abbreviation: S = simulated, M = measured.

4.3.2 Radiation Performances

In Fig. 4.7(a)-(b), the proposed antenna's simulated and measured 2-D radiation patterns are observed in two principal planes (xz- and yz-plane) at two representative frequencies

4.82 GHz and 11.45 GHz, when element-1 is excited, and other elements are kept matched terminated. The pattern shows significant co-to-cross polar isolation with an almost omnidirectional pattern. The measured 2-D radiation patterns of the antenna are in close agreement with the simulated.

Fig. 4.7(c) shows the simulated 3-D radiation patterns of the proposed antenna when element-1 is excited and the rest of the elements are kept matched terminated. The simulated peak gain of 3.6 dBi is observed at the frequency of 4.82 GHz. Interestingly, when all elements are excited at a time, 3-D omnidirectional patterns have nulls in the endfire direction. A 3-D radiation pattern at 4.82 GHz is demonstrated for brevity, and a simulated peak gain of 4.72 dBi is observed, as shown in Fig. 4.7(d).

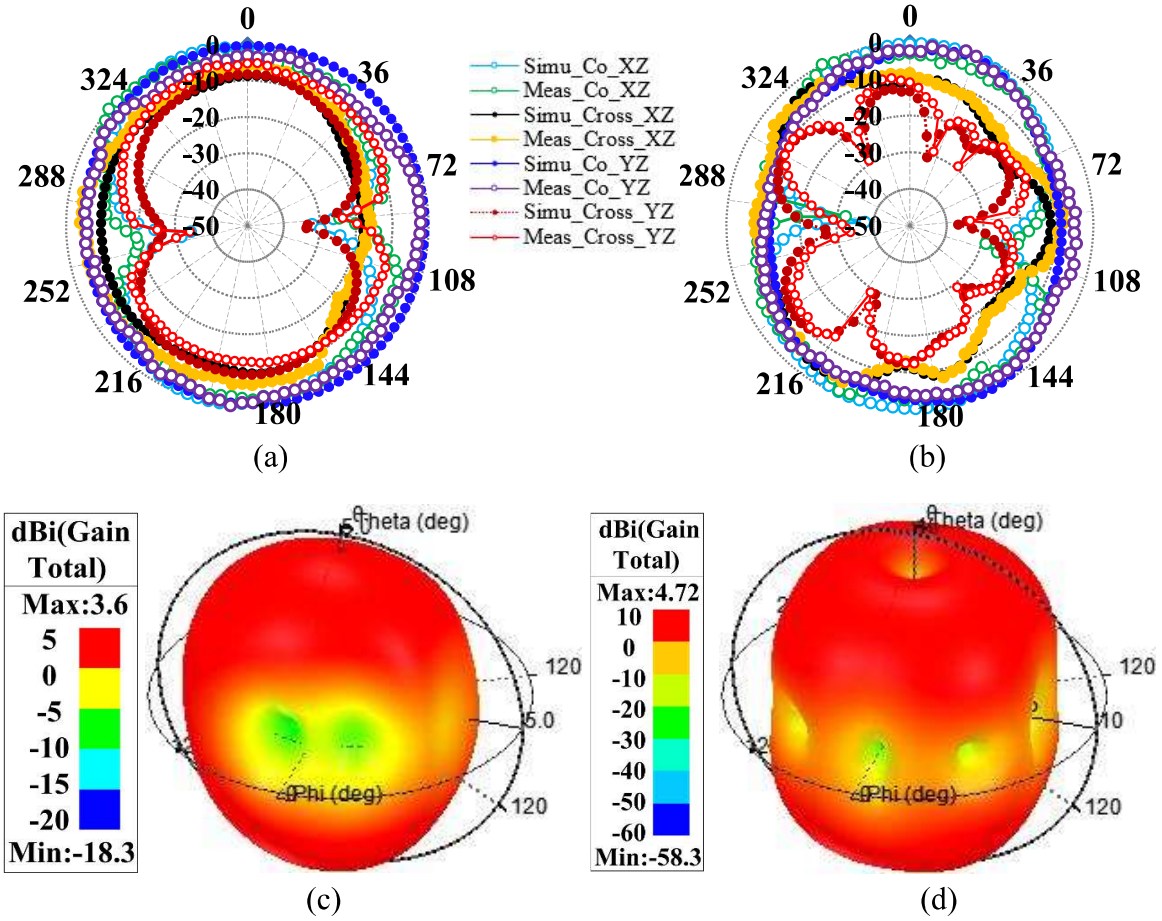

Fig. 4.7: Simulated and measured 2-D radiation patterns for element-1 along xz-plane and yz-plane (a) at 4.82 GHz and (b) at 11.45 GHz, (c) 3-D radiation pattern at 4.82 GHz, when element-1 is excited, and (d) when all elements are excited.

4.3.3 Gain and Efficiency

The simulated and measured peak realized gain of the proposed antenna are plotted in Fig. 4.8(a). It is observed that the realized gain of the proposed antenna rises with the rise in the frequency over the wideband and the value of gain is lies in range of 1.15-5.04 dBi.

The total efficiency of the i^{th} element and multiplexing efficiency of the N-element MIMO system are approximated in [21], [25]. The simulated plots of efficiencies (radiation, total, and multiplexing efficiency) of the proposed MIMO antenna are illustrated in Fig. 4.8(b). It is observed that the radiation efficiency and total efficiency of element-1 in the eight-element MIMO antenna are almost similar to the other elements (i.e., element-2, 3, 4, 5, 6, 7, and 8). The multiplexing efficiency of the proposed MIMO antenna is close to total efficiency due to the low value of correlation and identical efficiency. The efficiency of the proposed antenna decreases with the increase in the frequency over the wideband.

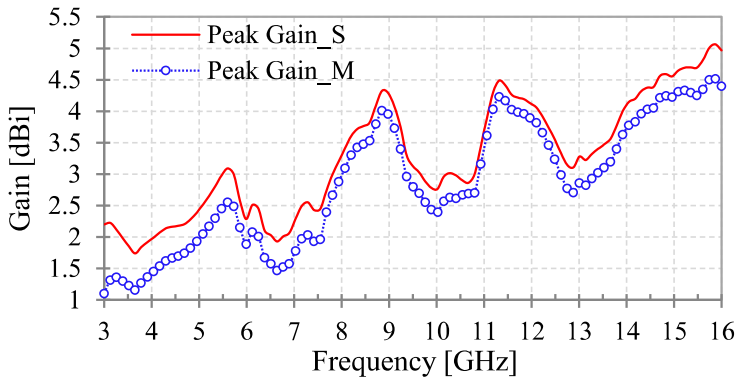

(a)

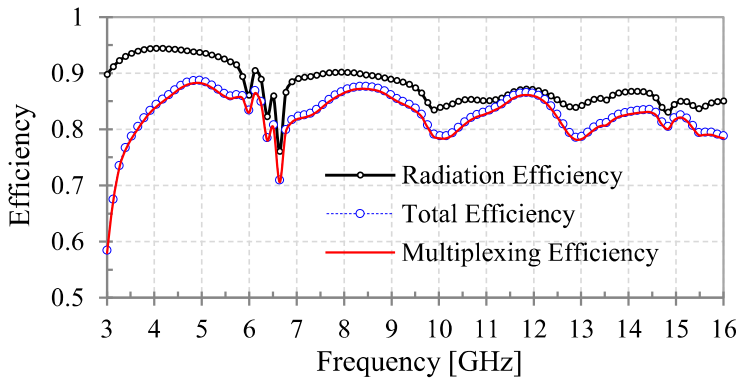

(b)

Fig. 4.8: Eight-element MIMO antenna (a) efficiency and (b) gain.

4.3.4 Diversity Performances (ECC and TARC)

To realize the correct behaviour of the MIMO antenna system, the study of the diversity parameters is a necessity for a practical scenario, which is analysed in the following sections. The envelope correlation coefficient (ECC) and active reflection coefficient (TARC) are approximated in [27].

A maximum value (simulated using *S*-parameters and 3D-field method and measured using *S*-parameters only) of ECC is 0.185 in the wideband, but from 3.3 GHz to 16 GHz, values are well below than 0.05, as shown in Fig. 4.9(a).

The TARC is estimated by exciting element_1 at unity amplitude and zero phase ($P^1=0^\circ$), while the rest all elements are excited by similar amplitude but different phases (varied from 0° to 360°) in seven different cases as Case-1 to Case7.

Case-1: $P^1=0^\circ$, $P^2=0^\circ$, $P^3=30^\circ$, $P^4=60^\circ$, $P^5=90^\circ$, $P^6=120^\circ$, $P^7=150^\circ$, $P^8=180^\circ$, Case-2: $P^1=0^\circ$, $P^2=30^\circ$, $P^3=60^\circ$, $P^4=90^\circ$, $P^5=120^\circ$, $P^6=150^\circ$, $P^7=180^\circ$, $P^8=210^\circ$, Case-3: $P^1=0^\circ$, $P^2=60^\circ$, $P^3=90^\circ$, $P^4=120^\circ$, $P^5=150^\circ$, $P^6=180^\circ$, $P^7=210^\circ$, $P^8=240^\circ$, Case-4: $P^1=0^\circ$, $P^2=90^\circ$, $P^3=120^\circ$, $P^4=150^\circ$, $P^5=180^\circ$, $P^6=210^\circ$, $P^7=240^\circ$, $P^8=270^\circ$, Case-5: $P^1=0^\circ$, $P^2=120^\circ$, $P^3=150^\circ$, $P^4=180^\circ$, $P^5=210^\circ$, $P^6=240^\circ$, $P^7=270^\circ$, $P^8=300^\circ$, Case-6: $P^1=0^\circ$, $P^2=150^\circ$, $P^3=180^\circ$, $P^4=210^\circ$, $P^5=240^\circ$, $P^6=270^\circ$, $P^7=300^\circ$, $P^8=330^\circ$, Case-7: $P^1=0^\circ$, $P^2=180^\circ$, $P^3=210^\circ$, $P^4=240^\circ$, $P^5=270^\circ$, $P^6=300^\circ$, $P^7=330^\circ$, $P^8=360^\circ$).

The values (simulated and measured) of TARC are well below than 0.41 in the operating wideband with minor discrepancies, as shown in Fig. 4.9(b).

4.3.5 Camparison and Review

To justify the advantages and issues considering the table data, the proposed design is compared with the previous proclaimed article of the eight-element UWB-MIMO antenna, as listed in Table 4.1. The design in [83], [85], and [111] are planar structures, while the rest are nonplanar. The placement of planar/low-profile antennas inside/outside

the devices is more convenient than nonplanar structures (3D). Most of the antenna structures proclaimed in the table have isolated ground planes except the structure in [111]. Using a discrete ground plane and separate PCBs is not convenient for embedding the host in numerous practical applications [122]. The design in [85] has a more complex structure with slightly compact than the proposed antenna, but it suffers from an isolated ground plane. In [111], two different sets of four-element UWB-MIMO antennas based on microstrip line and CPW fed are used to design an 8-port MIMO antenna. Still, it suffers from compactness, impedance bandwidth, notched-band characteristics, and peak gain compared to the proposed antenna. The design in [120] and [138] has more isolation value, but it has a thoughtful issue of discrete PCB and ground plane. In [120], a single element antenna is primarily designed, and antenna PCBs are arranged around the octagonal shaped polystyrene 3D-body. Similarly, 2-element antenna PCBs are placed around the cubic shaped polystyrene 3D-body in [138]. Therefore 8-element MIMO antenna has isolated PCBs along with a discrete ground plane. To resolve these issues, a compact ultra-wideband eight-element MIMO antenna is proposed, which gives better performances compared to other antennas listed in Table 4.1.

4.4 Details of 3D-MIMO System

The utility of the antennas in 3D system-in package is a significant concern for modern automotive vehicles.

4.4.1 Configuration of 32-Element MIMO Antenna

In a practical scenario, the placement of the antenna is also vital for the designer. Therefore, the proposed low-profile eight-element antenna (confi_1) [as discussed in section 4.2, Fig. 4.2(a)] is connected with asymmetrically large metallic sheet of size (30×96.7 mm^2) through a copper strip of 10×0.75 mm^2 to make a shared ground plane, as

illustrated in Fig. 4.10(a), which is referred as confi_2. The comparative study is carried out to see the effect of the extended ground plane on confi_1. Fig. 4.10(b) shows the variation of reflection coefficient with frequency for both confi_1 and confi_2. Insignificant effect of extended ground is observed on confi_2 throughout the band. However, improved impedance matching ($S_{ij} \in i=j$) is observed in the frequency range of 8-9.5 GHz. Similarly, the negligible impact of coupling *S*-parameters ($S_{ij} \in i \neq j$) are observed throughout the band.

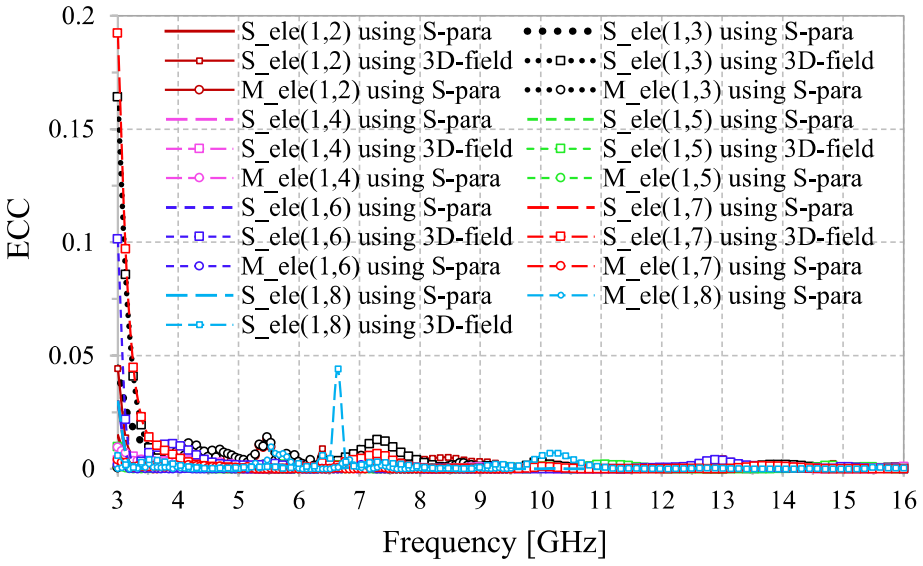

(a)

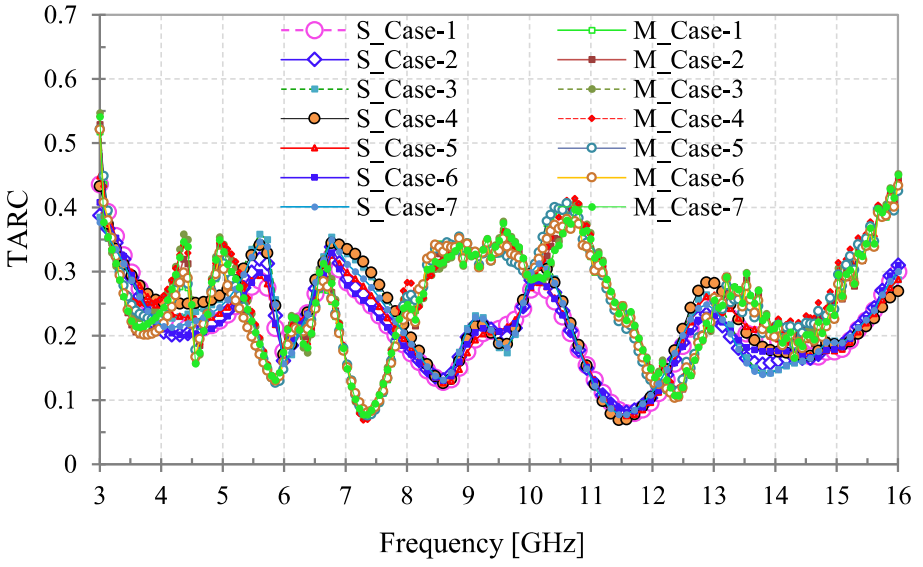

(b)

Fig. 4.9: Eight-element MIMO antenna (a) ECC and (b) TARC.

Table 4.1: Comparison data between the proposed antenna and other reported eight-element UWB-MIMO antenna

Ref.	**T_{PA}** L×W (λ_0^2)	**T_{AF}** L×W×H (10^{-3} λ_0^3)	**S_T** (mm)	**$A_{GP/PCB}$** (I/C)	**A_G** (P/N–P)	**IBW** -10dB (GHz)	**I_{Min}** (dB)	**G_P** (dBi)	**P_{3D}** (mm^3)
[83]	0.5958	6.1568	1.0	iso/com	pla	3.1–10.6	15	–	60×93×1.0
[85]	0.3420	2.6060	0.762	iso/com	pla	3–15	16	–	38×90×0.762
[136]	0.4693	117.50	1.6	iso/com	non-pla	2.9–12	16.5	–	38×90×0.762
[137]	0.25	66.310	1.524	iso/com	non-pla	3–11	15	–	50×50×26.524
[111]	0.7715	6.3775	0.8	com/com	pla	3.1–10.6	15	2–4.5/2–6.8	85×85×0.8
[120]	0.3222	106.55	1.5	iso/iso	non-pla	3.1–10.6	20	7	3017.77*×32
[138]	0.0723	18.813	1.6	iso/iso	non-pla	3–11	20	–	26.9×26×26.9
Prop.	0.4374	3.5339	0.8	com/com	pla	3.03–15.33	15.5	1.74–5.06	4287.5*×0.8

***Note*:** T_{PA} = total projection area, $\lambda_0 = c/f_0$ being highest operating wavelength (f_0 being lowest operating frequency), T_{AF} = total antenna footprint, S_T = substrate thickness, $A_{GP/PCB}$ = antenna ground plane/antenna printed circuit board (I = isolated/C = common), A_G = antenna geometry (P = planar/N–P = non–planar), IBW = -10 dB impedance bandwidth, I_{Min} = minimum isolation, P_G = peak gain, P_{3D} = 3D physical dimension, * = octagonal structure area in mm^2.

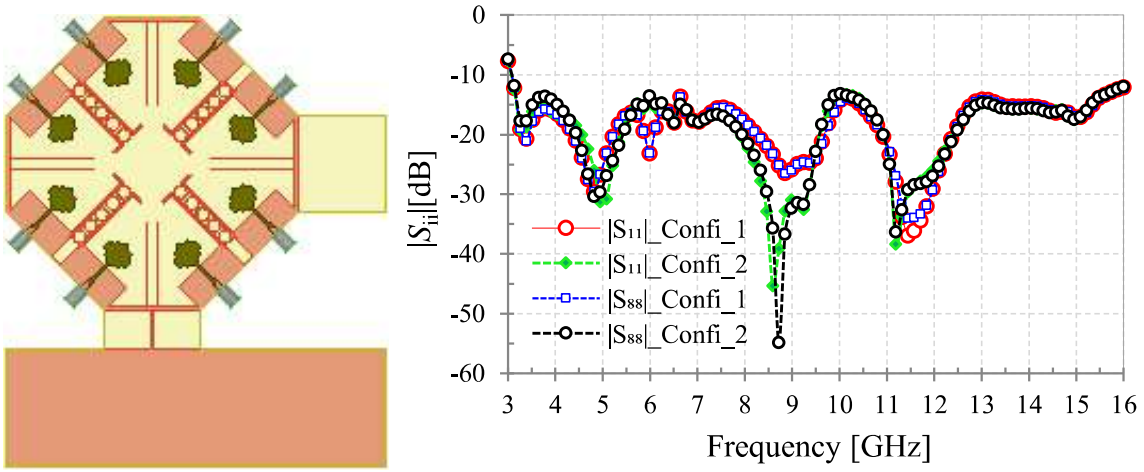

(a) (b)

Fig. 4.10: Eight-element MIMO antenna with large metallic sheet (a) confi_2 and (b) reflection coefficient of confi_1 and _2.

Further, confi_2 is considered as a unit cell for forming a higher-order (32-element) 3D-MIMO antenna for vehicular application. The 32-element 3D-MIMO antenna consists of four identical unit cells (namely, U^1, U^2, U^3, and U^4) of confi_2, which are placed orthogonally symmetrically rotated vertically around to central axis (x-axis) in y-x plane, as shown in Fig. 4.11(a). The unit cells U^1 and U^3 are etched on the same substrate board (y-x plane), but they are 180° out of phase from the central axis, as illustrated in Fig. 4.11(b). Similarly, U^2 and U^4 are placed on the same substrate board (z-x plane), but they are 180° out of phase from the central axis. The edge-to-edge distance between U^1 and U^3, U^2 and U^4 is $0.462\lambda_0$ (less than $\lambda_0/2$, λ_0 is at the lowest frequency) to reduce the mutual coupling between closely placed antenna elements. The proposed 3D-MIMO antenna is easily mounted on the vehicle roof-top, having zero connecting distance between them. The vehicle roof-top is chosen as a large metallic sheet of size 300×300 mm^2 for the simulation study. Further, the 3D-MIMO antenna structure is installed diagonally inside the acrylonitrile butadiene styrene ($\varepsilon_r = 2.3$) material-based cuboid house and placed on the vehicle's roof to check the antenna's capability in 3D system-in-package. The dimension of the cubic box is chosen as 142×142×115.25 mm^3, having 1 mm thickness based on the size of the 3D-MIMO antenna, as shown in Fig. 4.11(c).

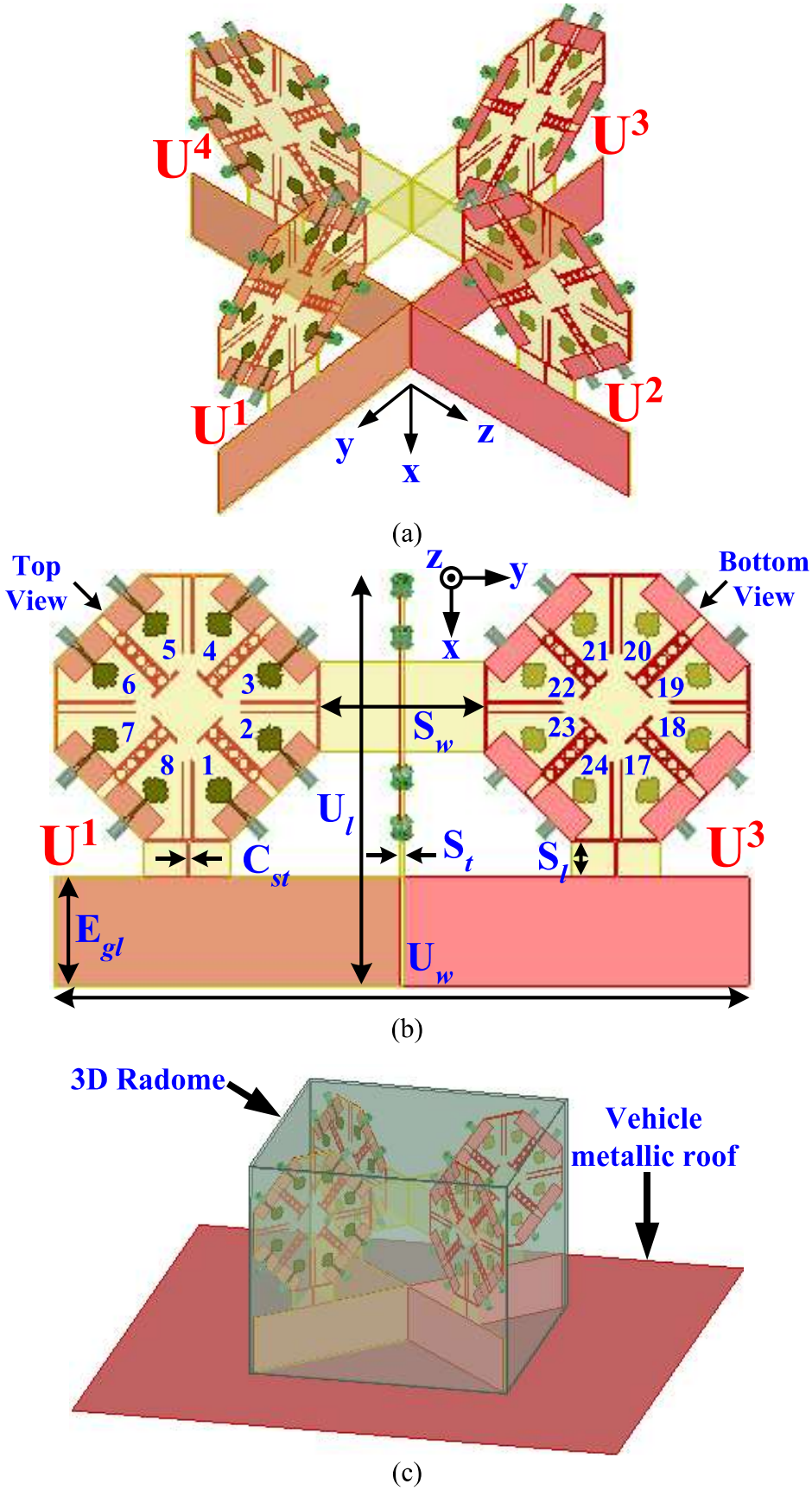

Fig. 4.11: 32-element 3D-MIMO system (a) overall 3D view (b) 2D front view of both unit cell U^1 and U^3, and (c) 3D view with radome and metallic sheet.
Dimensions (*in mm*): U_l=114.25, U_w=194.225, S_l=10, S_w=45.75, S_t=0.8, C_{st}=0.75, E_{gl}=30.

4.4.2 Results and Discussion

The performances of the proposed 32-element 3D-MIMO antenna are analyzed in the following sections.

4.4.2.1 *S*-parameters

The performances of the configured 32-element 3D-MIMO system without housing and with housing along with metallic sheet are analyzed, and S-parameters results of the 3D-MIMO system are plotted in Fig. 4.12(a)-(b). The proposed MIMO antenna considered in both cases successfully satisfied the essential criteria of practical applications, i.e., $S_{ij} \in i=j < -10$ dB (3.03-16 GHz) and $S_{ij} \in i \neq j < -15.5$ dB. The unit cells are interconnected in the 32-element 3D-MIMO system. As a result, the ground and substrate of each unit cell are asymmetrical for each element of the unit cell. Consequently, reflection coefficients for element-1 to 8 are slightly changed due to non-identical geometry for element-1 to element-8. All reflection coefficients are close to the $S_{ii} \in i=1$ to 8, and all transmission coefficients are almost similar to the $S_{ij} \in i \neq j$, $i=1$ to 8 and $j=1$ to 32; only essential coupling parameters are plotted here. The obtained results considered in both cases are almost identical, which shows the capability of the 3D-MIMO antenna in the 3D system-in-package.

4.4.2.2 Efficiency and Gain

The simulated total efficiency and peak realized gain for element-1 to element-8 of the 32-element 3D-MIMO antenna is plotted in Fig. 4.12(c) when one element is excited at a time, and the rest of the elements are kept matched terminated. It is observed that gain and efficiency are further enhanced compare to proposed eight-element MIMO antenna, the value of gain rises with rise the frequency in the respective band. Fig. 4.13 shows that the 3-D radiation pattern of the 32-element 3D-MIMO antenna along with housing and

metallic sheet at 8.2 GHz is demonstrated when all elements are excited at a time. A peak gain value of 10 dBi is observed at the same frequency.

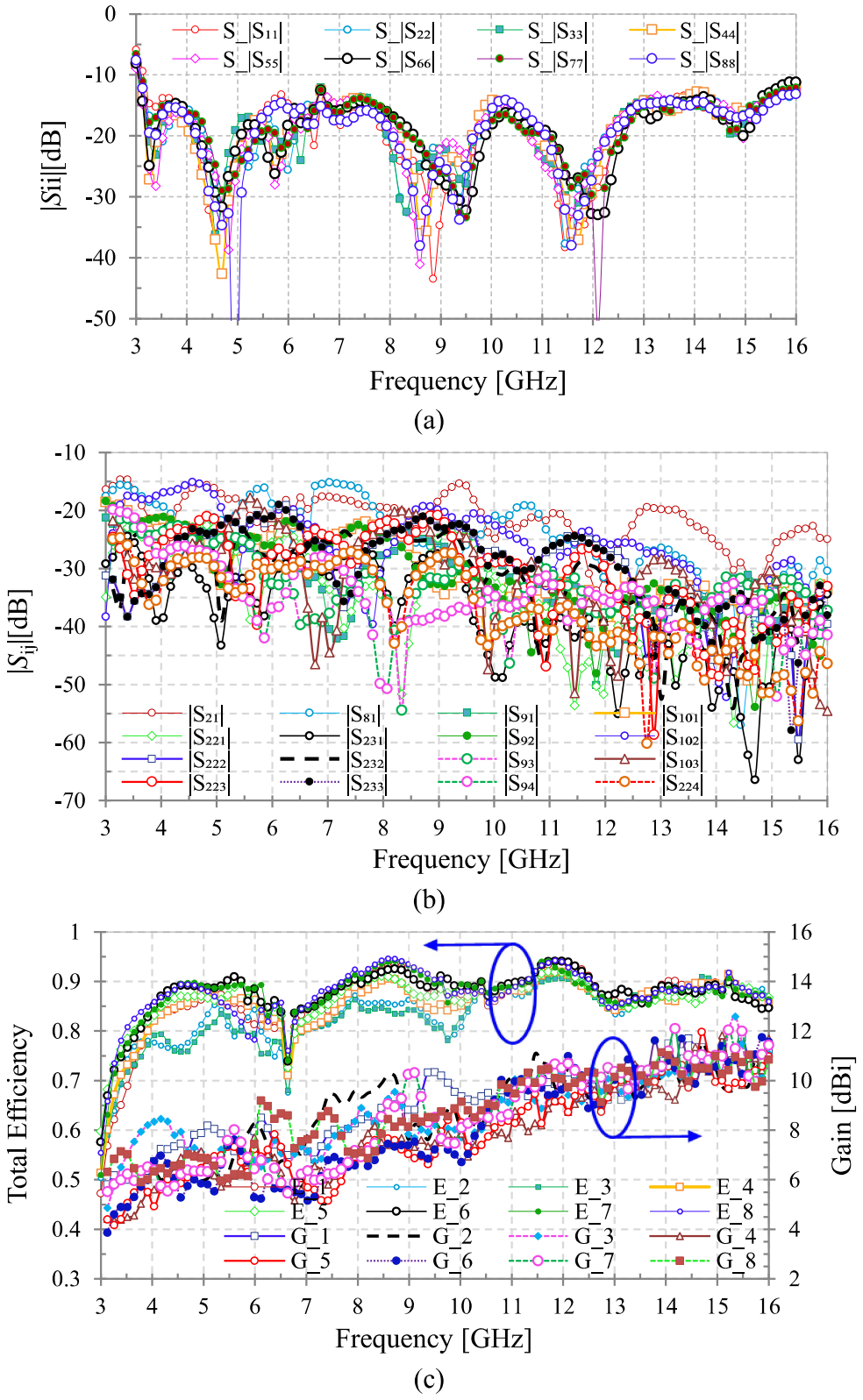

Fig. 4.12: 32-element 3D-MIMO system with radome and metallic sheet corresponding (a) reflection, (b) coupling *S*-parameter, and (c) total efficiency and peak realized gain. Abbreviation: E_1 and G_1 = radiation efficiency and peak realized gain of element-1.

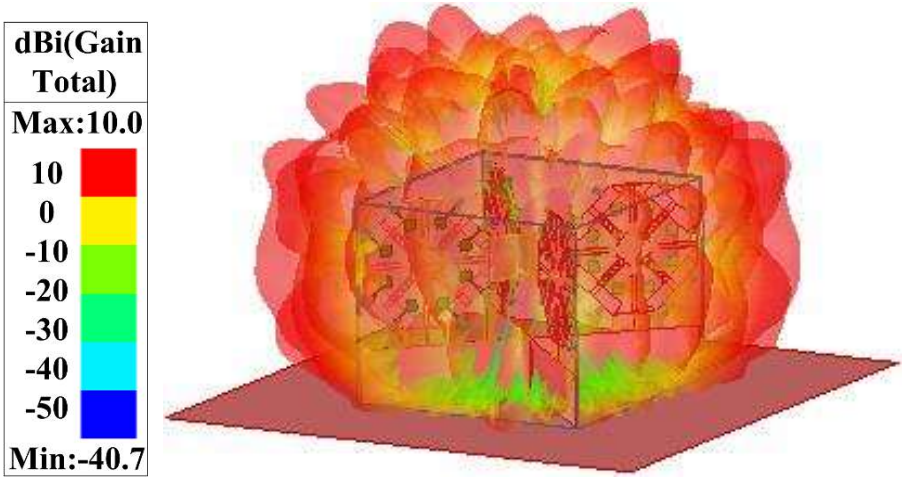

Fig. 4.13: 3D radiation pattern at 8.2 GHz of the 32-element 3D-MIMO system with radome and metallic sheet, when all elements are excited.

4.4.2.3 Comparison and Review

Based on table data, the proposed 3D-MIMO system is most appropriate compared to the listed MIMO designs in Table 4.2 because of the need for multiple antennas with good isolation with multiple communication bands working simultaneously. The antenna structure used in [133] is placed on the vehicle's metallic surface (having zero contacting distance), then its S-parameters results are observed to be relatively poor. Still, no significant effect of vehicle metallic surface on the proposed antenna is observed, which is another advantage of the present proposal.

Table 4.2: Comparison of the proposed 32-element MIMO antenna to similar vehicular MIMO antenna

Ref.	T_E	P_D	IBW	I_{min}	G_P	A_R
[127]	2	29×50×2.2	2.4-11	20	2	-
[128]	2	31350.08*×18	2.16-3.96	28.65	10.96	-
[130]	4	32×32×15	2.8-9.5	15	5.41	-
[131]	4	100×100×51.6	2.5-3.0	20	5	-
[133]	4	50×50×33.3	1.95-6.25	16.5	6.16	-
[134]	8	138.2×69.6×31.7	7.55-22.85	18.05	11.54	Yes
[139]	20	115×115×35.8	4.15-8.25	17	9.88	-
Pro.	32	142×142×114.25	3.03-16	15	12.1	Yes

$T_{E\text{-}N}$=total number of elements in MIMO structure, P_D=physical dimension in mm×mm×mm, IBW=-10 dB impedance bandwidth in GHz, I_{min}=minimum isolation in dB, G_P=peak gain in dBi, A_R=antenna radome, *Area of the circle.

4.5 Summary

In this chapter, a wideband compact/low-profile eight-element MIMO antenna is proposed for a higher-order vehicular MIMO system. It has a -10 dB measured fractional bandwidth of 133.98% (3.03-15.33 GHz) and a minimum isolation value of 15.5 dB throughout the wideband. The obtained satisfactory results (isolation, efficiency, gain, pattern, and diversity performances) of the proposed wideband eight-element MIMO antenna show that it is a competent candidate to realize a 32-element vehicular 3D-MIMO antenna for modern IoV communication (5G Sub-6 GHz/WLAN/V2X/V2V/V2I/V2S). The proposed 32-element 3D-MIMO antenna secured simulated $S_{ij} \in i=j < -10$ dB (3.03-16 GHz) and $S_{ij} \in i \neq j < -15.5$ dB, which is almost close to the eight-element MIMO antenna. The effects on that 3D-MIMO antenna with the radome and metallic roof are also studied, obtained satisfactory results show that it may be more appropriate for modern vehicular 3D system-in-package.

In next chapter 5, a ultra low-profile higher-order 5G-MIMO antenna is proposed for smartphone's back covers by integrating dual MIMO antenna on a common aperture. The proposed MIMO system in this investigation provides enhanced performances.